npj | quantum materials

Article

Published in partnership with Nanjing University

https://doi.org/10.1038/s41535-024-00650-6

Cubic double perovskites host noncoplanar spin textures

Joseph A. M. Paddison[1] ✉, Hao Zhang[2], Jiaqiang Yan[1], Matthew J. Cliffe[3], Michael A. McGuire[1], Seung-Hwan Do[1], Shang Gao[1,4], Matthew B. Stone[4], David Dahlbom[2], Kipton Barros[5], Cristian D. Batista[2] & Andrew D. Christianson[1] ✉

Magnetic materials with noncoplanar magnetic structures can show unusual physical properties driven by nontrivial topology. Topologically-active states are often multi-**q** structures, which are challenging to stabilize in models and to identify in materials. Here, we use inelastic neutron-scattering experiments to show that the insulating double perovskites Ba_2YRuO_6 and Ba_2LuRuO_6 host a noncoplanar 3-**q** structure on the face-centered cubic lattice. Quantitative analysis of our neutron-scattering data reveals that these 3-**q** states are stabilized by biquadratic interactions. Our study identifies double perovskites as a highly promising class of materials to realize topological magnetism, elucidates the stabilization mechanism of the 3-**q** state in these materials, and establishes neutron spectroscopy on powder samples as a valuable technique to distinguish multi-**q** from single-**q** states, facilitating the discovery of topologically-nontrivial magnetic materials.

Most magnetic materials order with simple magnetic structures in which spins are collinear or coplanar. Noncoplanar magnetic structures are relatively rare, but are of great current interest, because they can exhibit topological character and exotic physical properties[1,2]. For example, the finite scalar spin chirality of noncoplanar spin textures can generate a topological magneto-optical effect[3] and anomalous quantum Hall effect[4,5], even in the absence of spin-orbit coupling. Topologically-nontrivial spin textures are typically multi-**q** structures, which superpose magnetic modulations with symmetry-related wavevectors **q**[2]. Multi-**q** spin textures with long-wavelength modulations, such as skyrmion and hedgehog crystals, are well-studied as hosts of topology-driven phenomena[6–8]. In this context, multi-**q** antiferromagnets are increasingly important[9], because they offer higher densities of topological objects with the potential to generate stronger physical responses[10].

To probe the relationships between spin structure, interactions, topology, and physical response, it is crucial to identify real materials that host noncoplanar spin textures. This has proved a challenging task, for three main reasons. First, it is necessary to identify noncoplanar spin textures that are robust to subleading effects such as magnetic anisotropies, spin-lattice coupling[11,12], fluctuations[13–16], and anisotropic interactions[17], which usually favor collinear states. Second, most noncoplanar states are found in metals, such as USb[18,19] and γ-Mn alloys[20–25], and are often stable only under an applied magnetic field[6,26]. On the one hand, itinerant electrons can support the generation of physical responses; on the other hand, modeling the magnetic interactions of metals presents fundamental challenges[27–32], such that insulators are often more suitable as model materials. Third, neutron-diffraction measurements play a central role in solving magnetic structures, but suffer from a "multi-**q** problem": Such measurements are generally unable to distinguish 1-**q** from multi-**q** structures[33], due to orientational averaging for powders or domain averaging for single crystals. Therefore, multi-**q** spin textures are challenging to stabilize in models, and to identify in real materials.

Here, we identify the Mott-insulating double perovskites Ba_2YRuO_6 and Ba_2LuRuO_6[34–37] as prototypical examples of noncoplanar 3-**q** magnetism on the face-centered cubic (FCC) lattice in zero magnetic field. We obtain evidence for 3-**q** magnetism from a spin-wave analysis of neutron spectroscopy data. By optimizing the magnetic structure and interactions simultaneously against our data, we show that the 3-**q** structure is stabilized by biquadratic interactions within an antiferromagnetic Heisenberg-Kitaev model. Our study experimentally establishes that noncoplanar multi-**q** states are stabilized in frustrated FCC antiferromagnets, identifies cubic double perovskites as model materials to realize this behavior, and identifies guiding principles to facilitate design of materials with noncoplanar magnetic states.

[1]Materials Science and Technology Division, Oak Ridge National Laboratory, Oak Ridge, TN 37831, USA. [2]Department of Physics and Astronomy, University of Tennessee, Knoxville, TN 37996, USA. [3]School of Chemistry, University of Nottingham, Nottingham NG7 2RD, UK. [4]Neutron Scattering Division, Oak Ridge National Laboratory, Oak Ridge, TN 37831, USA. [5]Theoretical Division, Los Alamos National Laboratory, Los Alamos, NM 87545, USA.
✉e-mail: paddisonja@ornl.gov; christiansad@ornl.gov

Results

Theory and materials selection

Our study is motivated by theoretical results for the FCC antiferromagnet[13,38–41]. The nearest-neighbor Heisenberg-Kitaev spin Hamiltonian on the FCC lattice can be written as

$$H = J\sum_{\langle i,j\rangle} \mathbf{S}_i \cdot \mathbf{S}_j + K\sum_{\langle i,j\rangle_\gamma} S_i^\gamma S_j^\gamma, \quad (1)$$

where $\mathbf{S}_i$ is a Ru^{5+} spin with quantum number $S = 3/2$, J and K denote the Heisenberg and Kitaev interactions, respectively[39], and $\gamma \in \{x, y, z\}$ is perpendicular to the cubic face containing the bond between neighbors $\langle i, j\rangle$. For antiferromagnetic $J > 0$ only, the model is frustrated, and orderings with $\mathbf{q} \in [1, q, 0]$ are degenerate[13,40,41]. The degenerate manifold includes $\mathbf{q} = [1, 0, 0]$ ("Type I") ordering, which is favored by fluctuations[13,14,42] and is observed in Ba_2YRuO_6 and Ba_2LuRuO_6[34]. Henceforth, we therefore restrict our discussion to $\mathbf{q} = [1, 0, 0]$ ordering. For a collinear structure, spins may be either parallel or perpendicular to $\mathbf{q}$; the former is stabilized by $K < 0$ and the latter by $K > 0$[39–41].

Figure 1a shows the collinear (1-$\mathbf{q}$) and noncollinear (multi-$\mathbf{q}$) structures associated with Type I antiferromagnetism. An unusual property of the FCC lattice is that 1-$\mathbf{q}$, 2-$\mathbf{q}$, and 3-$\mathbf{q}$ structures are energetically degenerate for *all* bilinear interactions that stabilize Type I ordering[40,41]. Moreover, uniaxial anisotropy ($\sim S_z^2$) and antisymmetric exchange terms are forbidden by $Fm\bar{3}m$ symmetries, and quartic anisotropy ($\sim S_x^4 + S_y^4 + S_z^4$) is forbidden for $S = 3/2$ operators. Consequently, interactions that would usually favor collinear magnetic structures are inactive in the $S = 3/2$ FCC antiferromagnet. This remarkable property potentially allows noncollinear structures to appear.

To identify candidate systems for 3-$\mathbf{q}$ spin textures among the diverse magnetic ground states of double perovskites[43–51], we consider two criteria: Type I antiferromagnetic ordering, and strictly cubic symmetry below the magnetic ordering temperature, T_N. The second criterion is key because 3-$\mathbf{q}$ structures have cubic symmetry, while 1-$\mathbf{q}$ and 2-$\mathbf{q}$ structures have tetragonal or orthorhombic symmetry that could drive a crystallographic distortion *via* spin-lattice coupling [Fig. 1a]. We investigate Ba_2YRuO_6 and Ba_2LuRuO_6 because they are chemically well-ordered and show no evidence for low-temperature deviations from cubic symmetry[34,36]. Moreover, recent first-principles calculations predict that their magnetic structures might not be collinear[52], in apparent contradiction with interpretations of previous experiments[34].

Experiments

We prepared ~ 8 g polycrystalline samples of Ba_2YRuO_6 and Ba_2LuRuO_6 by solid-state reaction (see Methods). The magnetic ordering temperature $T_N \approx 37$ K is the same for both samples, and is suppressed compared to the Weiss temperature $\theta \sim -500$ K, indicating strong magnetic frustration[36]. Rietveld refinements to X-ray diffraction data confirm cubic symmetry above and below T_N (see Methods and Supplementary Fig. 1). The level of Y/Ru site mixing was undetectable (<3%) and Lu/Ru site mixing was 6(2)%, with minor impurity phases of ≈ 1 wt.% and ≈ 4 wt.% for M = Y and Lu, respectively (see Supplementary Table 1). We performed inelastic neutron-scattering measurements on the SEQUOIA instrument at ORNL[53] using incident neutron energies $E_i = 62$ and 11.8 meV, yielding elastic energy resolutions $\delta_{ins} \approx 1.68$ and 0.27 meV, respectively.

Rietveld refinements to elastic magnetic scattering

Figure 1b shows magnetic Rietveld refinements to our elastic neutron-scattering data measured at $T \approx 5$ K. Applying the $\mathbf{q} = [1, 0, 0]$ propagation vector to $Fm\bar{3}m$ crystal symmetry generates two magnetic irreducible representations (irreps), notated $m\mathrm{X}_3^+$ and $m\mathrm{X}_5^+$[54–57]. These irreps can be distinguished by their magnetic Bragg profiles. The $m\mathrm{X}_5^+$ irrep agrees well with our elastic-scattering data for both materials; Rietveld refinements yield ordered magnetic moment lengths of 2.56(2) and 2.43(2) μ_B per Ru for Ba_2YRuO_6 and Ba_2LuRuO_6, respectively. Since the Ru^{5+} magnetic form factor has not been accurately determined, we tested several 4*d* magnetic form factors[58]; while this choice does not qualitatively affect our results, the form factor for Zr^+ (isoelectronic with Ru^{5+}) yields optimal agreement with our data and is used throughout. The Zr^+ form factor also yielded better agreement with our data than the interpolated Ru^{5+} form factor used in ref. 59. In contrast to the $m\mathrm{X}_5^+$ irrep, the $m\mathrm{X}_3^+$ irrep strongly disagrees with our data, as it yields zero intensity for the strong (100) magnetic Bragg peak. This can be understood intuitively for a collinear 1-$\mathbf{q}$ structure, because neutrons are only sensitive to spin components perpendicular to the scattering wavevector, and the $m\mathrm{X}_3^+$ irrep has $\mathbf{S}\|\mathbf{q}$ while the $m\mathrm{X}_5^+$ irrep has $\mathbf{S} \perp \mathbf{q}$ [Fig. 1a]. A previous neutron-diffraction study of Ba_2YRuO_6 and Ba_2LuRuO_6 considered only collinear 1-$\mathbf{q}$ structures[34], but could not rule out multi-$\mathbf{q}$ structures, due to the multi-$\mathbf{q}$ problem.

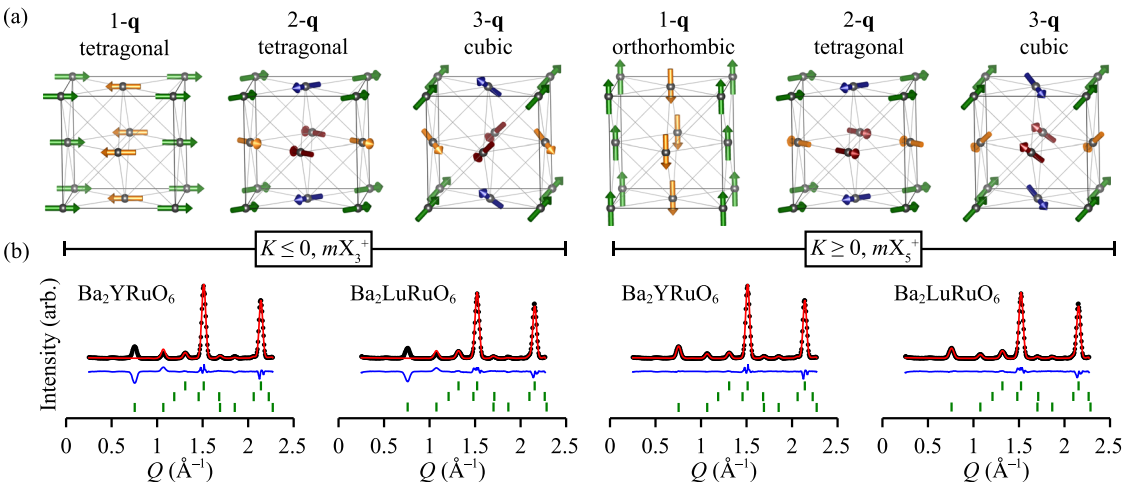

Fig. 1 | Candidate magnetic structures and powder neutron diffraction patterns. **a** Symmetry-allowed magnetic structures with propagation vector $\mathbf{q} = [1, 0, 0]$ on the FCC lattice for Ba_2MRuO_6 (space group $Fm\bar{3}m$; $a = 8.29$ and 8.24 Å for M = Y and Lu, respectively). The 1-$\mathbf{q}$, 2-$\mathbf{q}$, and 3-$\mathbf{q}$ structures are shown for the $m\mathrm{X}_3^+$ irrep (left) and the $m\mathrm{X}_5^+$ irrep (right). Spins along different directions are colored differently; note that 1-$\mathbf{q}$, 2-$\mathbf{q}$, and 3-$\mathbf{q}$ structures have [100], ⟨110⟩, and ⟨111⟩ spin directions, respectively. In ref. 52, these structures (left to right) are labeled E_{1a}, E_{2d}, E_{3c}, E_{1b}, E_{2a}, E_{3a}. **b** Elastic scattering data ($-1.3 \le E \le 1.3$ meV) measured at $T = 5$ K with $E_i = 11.8$ meV for Ba_2YRuO_6 and Ba_2LuRuO_6 (black circles), Rietveld refinements (red lines), and data–fit (blue lines). Tick marks show (top to bottom): nuclear, impurity M_2O_3, and magnetic phases. Note that the Rietveld refinements depend only on the irrep and are identical for 1-$\mathbf{q}$, 2-$\mathbf{q}$, and 3-$\mathbf{q}$ structures of the same irrep.

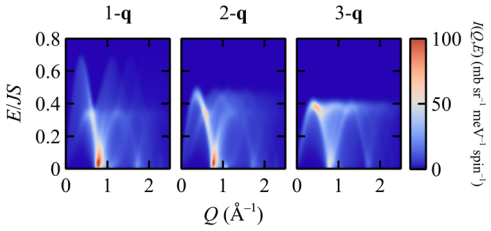

Fig. 2 | Calculated powder-averaged spin-wave spectra for candidate magnetic structures. Calculated spectra are shown for 1-**q**, 2-**q**, and 3-**q** structures (left to right) with the mX_5^+ irrep. Only antiferromagnetic Heisenberg J is included, and all other interactions are zero.

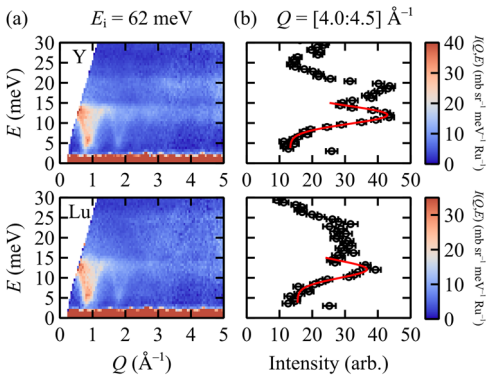

Fig. 3 | Broadband inelastic neutron-scattering data ($E_i = 62$ meV) measured at $T = 5$ K. Upper and lower panels show data for Ba_2YRuO_6 and Ba_2LuRuO_6, respectively. **a** Intensity as a color plot, and (**b**) energy dependence integrated over $4.0 \le Q \le 4.5$ Å^{-1}, where experimental data are shown as black circles, and Gaussian fits to the ~14 meV phonon band as red lines. Error bars in experimental data indicate 1 s.d.

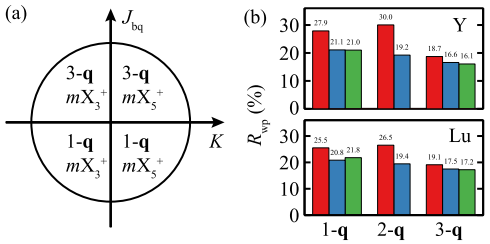

Fig. 4 | Phase diagram and goodness-of-fit for candidate magnetic structures. **a** Schematic phase diagram showing the magnetic ground states of the J-K-J_{bq} model. **b** Goodness-of-fit metric R_{wp} for candidate magnetic structures and interaction models of Ba_2YRuO_6 (upper graph) and Ba_2LuRuO_6 (lower graph). The graphs show R_{wp} for refinements of the Heisenberg-Kitaev (J-K) model including a third refined parameter Γ (red bars), J_2 (blue bars), or J_{bq} (green bars); note that the 2-**q** structure is stable only for $J_{bq} = 0$.

Overview of inelastic magnetic scattering

To overcome the multi-**q** problem, we consider the energy dependence of neutron-scattering data[60]. To explain this choice of approach, Fig. 2 shows calculated spin-wave spectra for the 1-**q**, 2-**q** and 3-**q** structures with the mX_5^+ irrep. Here, only antiferromagnetic Heisenberg interactions are included. Qualitative differences between the calculated powder-averaged spectra for 1-**q**, 2-**q** and 3-**q** structures are apparent; e.g., the 3-**q** calculation shows a cutoff of magnetic signal for energies above ~ 0.4JS, whereas the magnetic signal for the the 1-**q** calculation extends to ~ 0.7JS. These calculations motivate the use of powder-averaged inelastic neutron scattering data to distinguish between these candidate ground states, and will inform our discussion of the experimental spectra.

Figure 3a shows our experimental inelastic data measured with $E_i = 62$ meV at $T \approx 5$ K. A structured inelastic signal appears at $T < T_N$ for small scattering wavevectors, $Q \lesssim 2$ Å^{-1}, which we identify as magnon scattering. The magnon scattering is very similar for M = Y and Lu, except the features for M = Lu appear slightly broader, which may reflect the slightly greater degree of M/Ru site mixing in this compound (see Supplementary Fig. 1 and Supplementary Table 1). The top of the magnetic band overlaps with an intense phonon signal for $Q \gtrsim 2$ Å^{-1}. Figure 3b shows the scattering intensity integrated over $4.0 \le Q \le 4.5$ Å^{-1}, from which we extract the average energy E_{ph} and width σ_{ph} of this phonon band via Gaussian fits for each material. The energy overlap of magnon and phonon modes suggests that spin-lattice coupling may be significant, which we consider below.

Optimization of magnetic structure and Hamiltonian

Our starting point for modeling the magnetic scattering is the nearest-neighbor Heisenberg-Kitaev model, Eq. (1). Antiferromagnetic $J > 0$ has been shown to be important in Ba_2YRuO_6[37], and we include $K > 0$ because it is needed to stabilize magnetic ordering with the mX_5^+ irrep, as observed experimentally[34]. We consider three additional interactions. First, the symmetric off-diagonal interaction $H_\Gamma = \Gamma \sum_{\langle i,j \rangle_\gamma} (S_i^\alpha S_j^\beta + S_i^\beta S_j^\alpha)$ is the only additional bilinear nearest-neighbor interaction allowed by symmetry[39]. Second, the Heisenberg next-nearest neighbor interaction $H_2 = J_2 \sum_{\langle\langle i,j \rangle\rangle} \mathbf{S}_i \cdot \mathbf{S}_j$ has been invoked for Ba_2YRuO_6[37]; we require $J_2 \le 0$ to stabilize Type I ordering. Third, the nearest-neighbor biquadratic coupling $H_{bq} = J_{bq} \sum_{\langle i,j \rangle} (\mathbf{S}_i \cdot \mathbf{S}_j)^2$ has been invoked in density-functional-theory calculations for 4d double perovskites due to their increased electron hopping relative to 3d analogs[52]. While the 4-spin exchange enters into the Hamiltonian at the same order as biquadratic exchange, these terms can be combined for the FCC lattice[52], so we do not consider them separately. For $J_{bq} = 0$, the classical energy of 1-**q**, 2-**q**, and 3-**q** structures is equal for all K, Γ, and J_2 that stabilize Type I ordering. Nonzero J_{bq} removes this degeneracy and stabilizes 1-**q** ordering for $J_{bq} < 0$ and 3-**q** ordering for $J_{bq} > 0$ [Fig. 4a]. Importantly, since single-ion anisotropies are forbidden for $S = 3/2$ in a cubic environment, biquadratic exchange is the only physically-plausible mechanism that can remove the degeneracy of 1-**q** and 3-**q** structures.

We performed extensive fits to our inelastic neutron-scattering data to optimize the magnetic interactions for each candidate magnetic structure. For each structure associated with the mX_5^+ irrep (1-**q**, 2-**q**, or 3-**q**), we optimized three spin Hamiltonian parameters (J, K, and either Γ, J_2, or J_{bq}) against the broadband inelastic data shown in Fig. 5a and the energy dependence near the (100) magnetic Bragg position shown in Fig. 5b. The broadband inelastic data provides an overview of the key features of the spectrum, while the low-energy data provides information about the magnon gap, which is an important constraint as we discuss further below. The powder-averaged magnon spectrum was calculated within the established approach of linear spin-wave theory[61,62] using the SpinW program[63], updated to include J_{bq}[64]. We included a renormalization factor that takes into account higher-order corrections in the 1/S expansion, which is necessary to extract a correct value of J_{bq} since the unrenormalized theory would yield a value of J_{bq} that is 2.25 times too small[65]. The parameter values were optimized to minimize the sum of squared residuals using nonlinear least-squares refinement; our general approach is similar to[66–68]. For each refined model, several refinements were performed with different initial parameter values, to check for alternative χ^2 minima, and derivative-based and derivative-free optimizers were used (see Methods). An overall intensity scale factor was optimized in our refinements; we also optimized a linear-in-E intensity offset to account for phonon scattering. To account for magnon-phonon coupling, we calculated the energy-dependent broadening of the magnon spectrum as $\delta(E) = \delta_{ins}(E) + Ae^{-(E-E_{ph})^2/2\delta_{ph}^2}$, where $\delta(E)$ is the overall Gaussian energy width, $\delta_{ins}(E)$ is the instrumental resolution, and A is a refined parameter that phenomenologically accounts for magnon broadening due to coupling with phonons at $E \sim E_{ph}$.

Figure 5a compares our broadband inelastic data ($E_i = 62$ meV) with the best fit for each of the 1-**q**, 2-**q**, and 3-**q** structures. The data show two

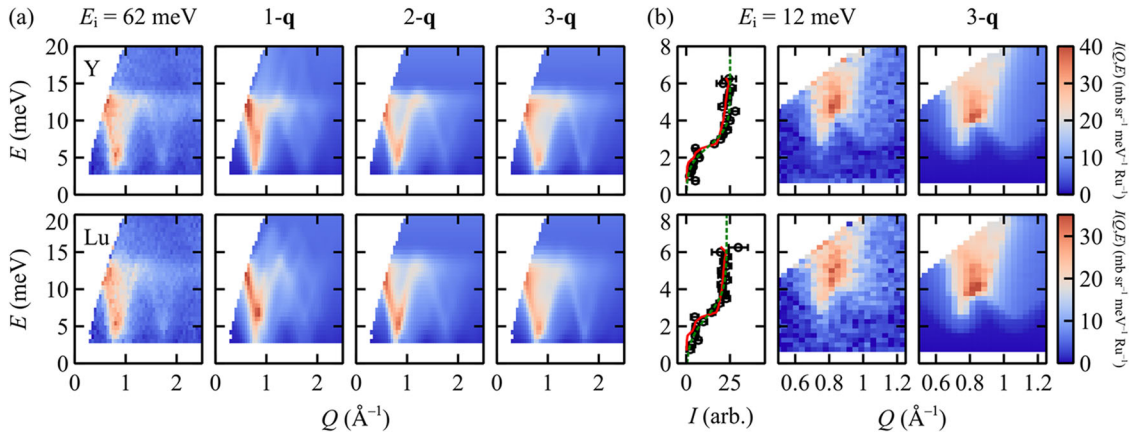

Fig. 5 | Inelastic neutron-scattering data and model fits. a Broadband inelastic neutron-scattering data (E_i = 62 meV) and spin-wave fits for different magnetic structures, showing (left to right) experimental data, 1-**q** fit, 2-**q** fit, and 3-**q** fit. Optimal fits are shown for each structure and correspond to the following models: J-K-J_{bq} (3-**q** structures and 1-**q** structure for M = Y) and J-K-J_2 (2-**q** structures and 1-**q** structure for M = Lu). **b** Low-energy inelastic neutron-scattering data (E_i = 11.8 meV) and 3-**q** model calculations, showing (left to right) a cut at $Q = 0.7450 \pm 0.0175$ Å^{-1} comparing experimental data (black circles), spin-wave fit (solid red lines) and fit to a sigmoid function defined in the text (dotted green lines); experimental data as a Q-E slice; and spin-wave calculation. Note that the maximum energy transfer is restricted to ≈ 6 meV at $Q = 0.745$ Å^{-1} by kinematic constraints. Error bars in experimental data indicate 1 s.d.

V-shaped features centered near the (100) and (120) magnetic Bragg peaks at ≈ 0.76 and ≈ 1.70 Å^{-1}, respectively, with a sharp cutoff of magnetic signal for energies above ~ 14 meV. For both materials, these characteristics are best reproduced by the 3-**q** structure, while the 1-**q** structure disagrees with our experimental data. These observations are confirmed by the goodness-of-fit metric R_{wp} [Fig. 4b]. For both materials and for every interaction model we considered, the 3-**q** structure yields better agreement with our data than the 1-**q** or 2-**q** structure. Notably, the goodness-of-fit is more sensitive to the structure than the precise magnetic interactions; indeed, the qualitative differences between 1-**q** and 3-**q** spectra are more apparent for Heisenberg exchange only [Fig. 2]. The global best fit is for the 3-**q** structure and J, K, and J_{bq} interactions with the refined values given in Table 1. Refined values of A indicate magnon broadening due to magnon-phonon coupling is larger for Ba_2LuRuO_6. Importantly, for both materials, the biquadratic term is significant, with $J_{bq}/J \sim 0.06$. Hence, our key results are that only the 3-**q** spin texture agrees well with our neutron data, and this state is stabilized by biquadratic interactions. Similar results for both materials suggest that this state is insensitive to a low level of chemical disorder, as is observed in Ba_2LuRuO_6 only (see Supplementary Fig. 1 and Supplementary Table 1).

Origin of magnon gap

Our model provides insight into the mechanism of gap opening[35]. Low-energy inelastic neutron scattering measurements (E_i = 11.8 meV) shown in Fig. 5b reveal gaps of 2.59(6) meV and 2.49(11) meV for M = Y and Lu, respectively, estimated by fits to a sigmoid function, $I(E) \propto 1/[1 + e^{-\sigma_g(E-E_g)}]$, where E_g and σ_g are the fitted gap energy and width, respectively. Figure 5b also compares our low-energy inelastic data with the 3-**q** magnon spectrum for the optimal J-K-J_{bq} model [Table 1]. This calculation reproduces the observed gap. In contrast, the J-K-J_2 model that yields the next-best R_{wp} does not yield a gap for any of the candidate magnetic structures, and can therefore be discounted (see Supplementary Fig. 2). Since single-ion anisotropies are forbidden here, the mechanism of gap opening is subtle. A fully isotropic model ($J > 0$ only) possesses gapless Goldstone modes and accidental zero-energy modes[42,69]. Both types of excitation must become gapped to explain the observed gap in neutron spectra, and whether this occurs depends on both structure and interactions. For a 1-**q** structure with **S**||**q** (stable for $J_{bq} < 0$ and $K < 0$), the spectrum is fully gapped[70]; however, this magnetic structure was ruled out by elastic neutron data [Fig. 1]. The 1-**q** structure with **S**⊥**q** (stable for $J_{bq} < 0$ and $K > 0$) is consistent with elastic neutron data, but its spectrum remains gapless for nonzero K because of the continuous rotational symmetry in the spin plane. By contrast, if the structure is 3-**q**, a gap is present at the linear spin-wave level if both $J_{bq} > 0$ and $K > 0$, since these interactions together favor ⟨111⟩ spin alignment. We conclude that it is difficult to explain the elastic neutron data and the observed gap with a 1-**q** structure. However, these observations can be explained by a 3-**q** model with $J_{bq} > 0$ and $K > 0$, which also yields optimal agreement with our high-energy inelastic neutron-scattering data.

Continuous symmetries and their associated gapless Goldstone modes are maintained when considering quantum effects beyond linear spin-wave theory, which may have a similar effect to negative J_{bq} by favoring collinear structures[71] and gapping the accidental zero-energy modes[42,70]. We note that the energy scale of quantum order-by-disorder is relatively small, on the order of $10^{-3}J$[42], and can be easily surpassed by the expected biquadratic exchange interaction in these materials. Ref. 52 suggests that the combined J_{bq} and 4-spin interaction is on the order of $0.1J$ for Ba_2YRuO_6, in reasonable agreement with our own fits. Importantly, this J_{bq} value results in an energy difference between 1-**q** and 3-**q** orderings that is much larger than any energy difference induced by order by disorder.

Table 1 | Refined values of magnetic interaction parameters for the J-K-J_{bq} model and 3-q structure

	J (K)	K (K)	J_{bq} (K)	A (meV)
Ba_2YRuO_6	21.85 (3)	0.39 (1)	1.32 (2)	0.97 (3)
Ba_2LuRuO_6	22.27 (4)	0.36 (2)	1.17 (3)	2.25 (5)

Uncertainties indicate 1σ statistical confidence intervals.

Discussion

We have identified Ba_2YRuO_6 and Ba_2LuRuO_6 as model materials that host noncoplanar 3-**q** structures stabilized by biquadratic interactions in zero applied field. Macroscopic topological physical responses may be generated synthesizing thin films of these materials with [111] strain[72]. Our experimental results strikingly confirm recent first-principles predictions[52]. The positive sign of J_{bq} suggests that the effect of inter-site electron hopping outweighs spin-lattice coupling, since the latter would give a negative contribution to J_{bq}[11,12]. Crucially, we quantify the interactions that stabilize the noncoplanar state, in contrast to proposed 3-**q** structures in NiS_2[73–75], $MnTe_2$[76], and UO_2[77–80], where the relevant interactions are not yet well understood. Our work provides guiding principles to facilitate the identification of multi-**q** spin textures. First, double perovskites offer a rich materials space in which 1-**q** and multi-**q** structures may be nearly degenerate on the FCC lattice. In candidate materials, the crystal symmetry should

be higher than a 1-**q** model would imply. Second, magnets that are not deep inside the Mott-insulating regime are expected to have larger J_{bq} and, consequently, more robust 3-**q** orderings. This criterion hints that cubic Ba_2YOsO_6[81,82] may also host a 3-**q** state, due to its extended Os 5*d* orbitals, potentially offering a route to investigate the effect of increased electron hopping. For small J_{bq}, we anticipate a thermally-induced transition from 3-**q** to 1-**q** ordering, since thermal fluctuations favor collinear states. Third, quartic single-ion anisotropy may play a role in FCC magnets with $S > 3/2$; in particular, easy-⟨111⟩ axis anisotropy should favor 3-**q** ordering. The relevance of 3-**q** ordering extends beyond the FCC lattice: two themes are the presence of 3-fold or 6-fold symmetries, such as in triangular, honeycomb, and kagome lattices, and the presence of higher-order interactions than Heisenberg exchange, such as biquadratic[83,84] and ring exchange terms[85]. A methodological insight that may be relevant for several lattices[60] is that established spin-wave methods can distinguish 1-**q** and multi-**q** structures by optimizing structure and interactions simultaneously. This result highlights that neutron-scattering experiments on bulk polycrystalline insulators are complementary to approaches such as γ-ray emission spectroscopy[21] and scanning-tunneling spectroscopies on conducting or thin-film materials[86].

Methods

Sample preparation and characterization

Polycrystalline samples were prepared by conventional solid state reactions[35]. Rare-earth oxides and RuO_2 powder were first dried at 900 °C overnight. A stoichiometric mixture of $BaCO_3$, M_2O_3 (M = Ba or Lu), and RuO_2 was thoroughly mixed, pelletized, and fired at 1315 °C for a week with intermittent regrinding. Magnetic properties were measured with a Quantum Design Magnetic Property Measurement System in the temperature range $2 < T < 300$ K. The temperature dependence of magnetization suggests both compounds order antiferromagnetically below ~ 37 K, consistent with refs. 34–36.

Neutron scattering data

Inelastic neutron-scattering data ($E_i = 60$ and 11.8 meV) were corrected for detector efficency using a vanadium standard, for absorption, and for background scattering by subtraction of empty-container measurements. The data were placed in absolute intensity units (mb meV^{-1} Ru^{-1}) by normalization to the nuclear Bragg profile.

Rietveld refinements were performed using the Fullprof program[87,88]. The peak-shape was modeled as a Gaussian with $H^2 = (U\tan^2\theta + W)^2$, where H is the full-width at half-maximum of the peak, and U and W are refined parameters[89]. We also refined the cell parameter, oxygen position parameter, magnetic moment length, intensity scale factor, zero offset, and fourth-order polynomial background terms, and a scale factor for the Y_2O_3 or Lu_2O_3 impurity phase. Atomic displacement parameters were neglected due to the low sample temperature and limited Q-coverage of the data.

X-ray diffraction data

X-ray diffraction data were collected at 20 K and 300 K on portions of the same samples measured by neutrons, using a Panalytical XPert Pro diffractometer and Cu Kα radiation ($\lambda = 1.540598$ Å, Ge(111) monochromator). The Bragg-Brentano geometry was used. The low-temperature collection used an Oxford Phenix cryostat.

Rietveld refinements were performed using the Fullprof program[87,88]. The peak-shape was modeled using a pseudo-Voigt function, with refined U, V, W, X and η_0 parameters, and four refined asymmetry parameters. Background was modeled using 6th-order Chebychev polynomials. Sample displacement and micro-absorption corrections were refined. Reflections from the Al sample holder were fitted using LeBail profile matching.

We obtained excellent agreement between refined and experimental profiles within the published cubic $Fm\bar{3}m$ model[34] at 20 K and 300 K (see Supplementary Fig. 1). No peak splitting or selective broadening was observed. This result confirms that Ba_2LuRuO_6 and Ba_2YRuO_6 are cubic above and below T_N, in agreement with previous studies[34,36].

The level of chemical disorder and impurity phases were quantified using Rietveld refinements. Refined values of all structural parameters are given in Supplementary Table 1, including the level of M/Ru site mixing, an overall atomic-displacement (B_{iso}) factor, and the oxygen position parameter x. Two minor impurity phases were identified: M_2O_3 (0.34(3) wt.% for M=Y, 0.93(9) wt.% for M=Lu) and $Ba_3MRu_2O_9$ (0.71(10) wt.% for M=Y, 2.6(4) wt.% for M=Lu). The value of B_{iso} is larger for Ba_2LuRuO_6 than for Ba_2YRuO_6, in agreement with ref. 34. In Ba_2YRuO_6, the level of Y/Ru site mixing refines to zero with an uncertainty of a few percent, consistent with previous high-sensitivity ^{89}Y magic-angle-spinning NMR measurements[36]. In Ba_2LuRuO_6, we refined a small but nonzero amount of Lu/Ru site mixing of 6(2)%. As discussed in ref. 36, the difference of x from $x = \frac{1}{4}$ is an indicator of the level of site ordering. As such, the values of x reported in Supplementary Table 1 are consistent with slightly increased site mixing for M=Lu compared with M=Y, which may also be reflected in the larger B_{iso} for M=Lu.

Spin-wave model fitting

Refinements were performed against two inelastic neutron-scattering data sets simultaneously: a slice with $0.3 \le Q \le 2.5$ Å^{-1} and $2.5 \le E \le 20$ meV ($E_i = 60$ meV data), and a cut at $Q = 0.7450 \pm 0.0175$ Å^{-1} with $0.75 \le E \le 6.25$ meV ($E_i = 11.8$ meV data). All data points were weighted by their uncertainties as $1/\sigma^2$. We minimized the function

$$\chi^2 = \sum_{Q,E} \left[\frac{I_{expt}(Q,E) - sI_{calc}(Q,E) - bE}{\sigma(Q,E)} \right]^2, \quad (2)$$

where subscript "expt" and "calc" indicate measured and calculated magnon spectra, respectively, σ is an experimental uncertainty, s is a refined overall scale factor, and b is a refined linear-in-E background term; it is assumed that s and b are equal for both data sets. To account for the instrumental resolution, calculations were convoluted with an energy-dependent Gaussian energy broadening (elastic FWHM = 1.68 and 0.27 meV for $E_i = 62$ and 11.8 meV, respectively) and a constant Gaussian Q-broadening (FWHM = 0.08 and 0.054 Å^{-1} for $E_i = 62$ and 11.8 meV, respectively). The parameter values were optimized using the Minuit nonlinear least-squares program using its derivative-based MIGRAD and derivative-free SIMPLEX algorithms[90,91]. For each refined model, at least four separate refinements were performed with different initial parameter values, to check for alternative χ^2 minima. Notably, minima with similar overall χ^2 were found for the 3-**q** structure with J, K and J_{bq} interactions. These minima corresponded to smaller values of K, which has a noticeable effect on the magnon spectra only at low energies. These minima yield a magnon gap that is significantly smaller than the observed gap, and were therefore neglected.

Data availability

Experimental data and simulation results supporting this study are available from the corresponding authors on reasonable request.

Code availability

Custom codes used in this study are available from the corresponding authors on reasonable request.

Received: 16 August 2023; Accepted: 19 April 2024;
Published online: 06 June 2024

References

1. Tokura, Y. & Kanazawa, N. Magnetic skyrmion materials. *Chem. Rev.* **121**, 2857–2897 (2021).
2. Shindou, R. & Nagaosa, N. Orbital ferromagnetism and anomalous Hall effect in antiferromagnets on the distorted fcc lattice. *Phys. Rev. Lett.* **87**, 116801 (2001).

3. Feng, W. et al. Topological magneto-optical effects and their quantization in noncoplanar antiferromagnets. *Nat. Commun.* **11**, 118 (2020).
4. Sürgers, C., Fischer, G., Winkel, P. & Löhneysen, H. V. Large topological Hall effect in the non-collinear phase of an antiferromagnet. *Nat. Commun.* **5**, 3400 (2014).
5. Zhou, J. et al. Predicted quantum topological Hall effect and noncoplanar antiferromagnetism in $K_{0.5}RhO_2$. *Phys. Rev. Lett.* **116**, 256601 (2016).
6. Kurumaji, T. et al. Skyrmion lattice with a giant topological Hall effect in a frustrated triangular-lattice magnet. *Science* **365**, 914–918 (2019).
7. Hirschberger, M. et al. Skyrmion phase and competing magnetic orders on a breathing kagome lattice. *Nat. Commun.* **10**, 5831 (2019).
8. Hirschberger, M. et al. Topological Nernst effect of the two-dimensional skyrmion lattice. *Phys. Rev. Lett.* **125**, 076602 (2020).
9. Gao, S. et al. Fractional antiferromagnetic skyrmion lattice induced by anisotropic couplings. *Nature* **586**, 37–41 (2020).
10. Gomonay, O., Baltz, V., Brataas, A. & Tserkovnyak, Y. Antiferromagnetic spin textures and dynamics. *Nat. Phys.* **14**, 213–216 (2018).
11. Penc, K., Shannon, N. & Shiba, H. Half-magnetization plateau stabilized by structural distortion in the antiferromagnetic Heisenberg model on a pyrochlore lattice. *Phys. Rev. Lett.* **93**, 197203 (2004).
12. Wang, F. & Vishwanath, A. Spin phonon induced collinear order and magnetization plateaus in triangular and kagome antiferromagnets: applications to $CuFeO_2$. *Phys. Rev. Lett.* **100**, 077201 (2008).
13. Gvozdikova, M. V. & Zhitomirsky, M. E. A Monte Carlo study of the first-order transition in a Heisenberg fcc antiferromagnet. *J. Exp. Theor. Phys. Lett.* **81**, 236–240 (2005).
14. Schick, R., Ziman, T. & Zhitomirsky, M. E. Quantum versus thermal fluctuations in the fcc antiferromagnet: Alternative routes to order by disorder. *Phys. Rev. B* **102**, 220405 (2020).
15. Singh, R. R. P., Zheng, W., Oitmaa, J., Sushkov, O. P. & Hamer, C. J. Symmetry breaking in the collinear phase of the J_1-J_2 Heisenberg model. *Phys. Rev. Lett.* **91**, 017201 (2003).
16. McClarty, P. A., Stasiak, P. & Gingras, M. J. P. Order-by-disorder in the *xy* pyrochlore antiferromagnet. *Phys. Rev. B* **89**, 024425 (2014).
17. Maksimov, P. A., Zhu, Z., White, S. R. & Chernyshev, A. L. Anisotropic-exchange magnets on a triangular lattice: Spin waves, accidental degeneracies, and dual spin liquids. *Phys. Rev. X* **9**, 021017 (2019).
18. Jensen, J. & Bak, P. Spin waves in triple-**q** structures: Application to USb. *Phys. Rev. B* **23**, 6180–6183 (1981).
19. Hälg, B. & Furrer, A. Anisotropic exchange and spin dynamics in the type-I (-IA) antiferromagnets CeAs, CeSb, and USb: A neutron study. *Phys. Rev. B* **34**, 6258–6279 (1986).
20. Hirai, K. & Jo, T. Triple-**q** and single-**q** states in antiferromagnetic fcc transition metals with the first-kind ordering. *J. Phys. Soc. Jpn* **54**, 3567–3570 (1985).
21. Kawarazaki, S. et al. Direct evidence for triple-**q** spin-density wave in fcc antiferromagnetic Mn-Ni alloy. *Phys. Rev. Lett.* **61**, 471–474 (1988).
22. Kawarazaki, S., Sasaki, Y., Yasuda, K., Mizusaki, T. & Hirai, A. The triple-**q** spin-density wave in the face-centred cubic antiferromagnetic $Fe_{54}Mn_{46}$ alloy. *J. Phys. Condens. Matter* **2**, 5747–5752 (1990).
23. Long, M. W. & Moze, O. Magnetic diffuse scattering and the triple-**q** structure in FCC γ-MnNi. *J. Phys. Condens. Matter* **2**, 6013–6030 (1990).
24. Fishman, R. S. et al. Structural and magnetic phase transitions in Mn-Ni alloys. *Phys. Rev. B* **61**, 12159–12168 (2000).
25. Hanke, J.-P., Freimuth, F., Blügel, S. & Mokrousov, Y. Prototypical topological orbital ferromagnet γ-FeMn. *Sci. Rep.* **7**, 41078 (2017).
26. Khanh, N. D. et al. Nanometric square skyrmion lattice in a centrosymmetric tetragonal magnet. *Nat. Nanotechnol.* **15**, 444–449 (2020).
27. Agterberg, D. F. & Yunoki, S. Spin-flux phase in the Kondo lattice model with classical localized spins. *Phys. Rev. B* **62**, 13816–13819 (2000).
28. Hayami, S. & Motome, Y. Multiple-**q** instability by $(d-2)$-dimensional connections of Fermi surfaces. *Phys. Rev. B* **90**, 060402 (2014).
29. Jo, T. On the possibility of the multiple spin density wave state in the first-kind antiferromagnetic FCC metals. *J. Phys. F Met. Phys.* **13**, L211–L216 (1983).
30. Matsuura, Y. & Jo, T. Theory of multiple spin density wave and lattice distortion in fcc antiferromagnets. *J. Phys. Soc. Jpn* **78**, 124709 (2009).
31. Hayami, S. & Motome, Y. Noncoplanar multiple-**q** spin textures by itinerant frustration: Effects of single-ion anisotropy and bond-dependent anisotropy. *Phys. Rev. B* **103**, 054422 (2021).
32. Hayami, S. & Motome, Y. Topological spin crystals by itinerant frustration. *J. Phys. Condens. Matter* **33**, 443001 (2021).
33. Kouvel, J. & Kasper, J. Long-range antiferromagnetism in disordered Fe-Ni-Mn alloys. *J. Phys. Chem. Solids* **24**, 529–536 (1963).
34. Battle, P. & Jones, C. The crystal and magnetic structures of Sr_2LuRuO_6, Ba_2YRuO_6, and Ba_2LuRuO_6. *J. Solid State Chem.* **78**, 108–116 (1989).
35. Carlo, J. P. et al. Spin gap and the nature of the $4d^3$ magnetic ground state in the frustrated fcc antiferromagnet Ba_2YRuO_6. *Phys. Rev. B* **88**, 024418 (2013).
36. Aharen, T. et al. Magnetic properties of the $S=\frac{3}{2}$ geometrically frustrated double perovskites La_2LiRuO_6 and Ba_2YRuO_6. Phys. Rev. B 80, 134423 (2009).
37. Nilsen, G. J., Thompson, C. M., Ehlers, G., Marjerrison, C. A. & Greedan, J. E. Diffuse magnetic neutron scattering in the highly frustrated double perovskite Ba_2YRuO_6. *Phys. Rev. B* **91**, 054415 (2015).
38. Yamamoto, Y. & Nagamiya, T. Spin arrangements in magnetic compounds of the rocksalt crystal structure. *J. Phys. Soc. Jpn.* **32**, 1248–1261 (1972).
39. Cook, A. M., Matern, S., Hickey, C., Aczel, A. A. & Paramekanti, A. Spin-orbit coupled $j_{\rm eff}=1/2$ iridium moments on the geometrically frustrated fcc lattice. *Phys. Rev. B* **92**, 020417 (2015).
40. Balla, P., Iqbal, Y. & Penc, K. Degenerate manifolds, helimagnets, and multi-**q** chiral phases in the classical Heisenberg antiferromagnet on the face-centered-cubic lattice. *Phys. Rev. Res.* **2**, 043278 (2020).
41. Diop, S.-S., Jackeli, G. & Savary, L. Anisotropic exchange and noncollinear antiferromagnets on a noncentrosymmetric fcc half-Heusler structure. *Phys. Rev. B* **105**, 144431 (2022).
42. Schick, R. et al. Ground state selection by magnon interactions in the fcc antiferromagnet. *Phys. Rev. B* **106**, 094431 (2022).
43. Gangopadhyay, S. & Pickett, W. E. Interplay between spin-orbit coupling and strong correlation effects: Comparison of the three osmate double perovskites Ba_2AOsO_6 (A = Na, Ca, Y). *Phys. Rev. B* **93**, 155126 (2016).
44. Paramekanti, A. et al. Spin-orbit coupled systems in the atomic limit: Rhenates, osmates, iridates. *Phys. Rev. B* **97**, 235119 (2018).
45. Bos, J.-W. G. & Attfield, J. P. Magnetic frustration in (LaA)$CoNbO_6$ (A = Ca, Sr, and Ba) double perovskites. *Phys. Rev. B* **70**, 174434 (2004).
46. Taylor, A. E. et al. Spin-orbit coupling controlled ground state in Sr_2ScOsO_6. *Phys. Rev. B* **93**, 220408 (2016).
47. Taylor, A. E. et al. Origin of magnetic excitation gap in double perovskite Sr_2FeOsO_6. *Phys. Rev. B* **98**, 214422 (2018).
48. Gao, S. et al. Antiferromagnetic long-range order in the $5d^1$ double-perovskite Sr_2MgReO_6. *Phys. Rev. B* **101**, 220412 (2020).
49. Paramekanti, A., Maharaj, D. D. & Gaulin, B. D. Octupolar order in d-orbital Mott insulators. *Phys. Rev. B* **101**, 054439 (2020).
50. Maharaj, D. D. et al. Octupolar versus Néel order in cubic $5d^2$ double perovskites. *Phys. Rev. Lett.* **124**, 087206 (2020).

51. Iwahara, N., Vieru, V. & Chibotaru, L. F. Spin-orbital-lattice entangled states in cubic d^1 double perovskites. *Phys. Rev. B* **98**, 075138 (2018).
52. Fang, Y.-W., Yang, R. & Chen, H. The complex non-collinear magnetic orderings in Ba_2YOsO_6: A new approach to tuning spin-lattice interactions and controlling magnetic orderings in frustrated complex oxides. *J. Phys. Condens. Matter* **31**, 445803 (2019).
53. Granroth, G. E. et al. SEQUOIA: A newly operating chopper spectrometer at the SNS. *J. Phys. Conf. Ser.* **251**, 012058 (2010).
54. Cracknell, A. P., Davies, B. L., Miller, S. C. & Love, W. F. Kronecker Product Tables. General Introduction and Tables of Irreducible Representations of Space Groups, vol. 1 (Plenum, 1979).
55. Wills, A. Magnetic structures and their determination using group theory. *J. Phys. IV France* **11**, 133–158 (2001).
56. Campbell, B. J., Stokes, H. T., Tanner, D. E. & Hatch, D. M. *ISODISPLACE*: A web-based tool for exploring structural distortions. *J. Appl. Crystallogr.* **39**, 607–614 (2006).
57. Stokes, H. T., Hatch, D. M. & Campbell, B. J. *ISODISTORT*, ISOTROPY software suite, iso.byu.edu.
58. Brown, P. J. *International Tables for Crystallography*, vol. C, chap. Magnetic Form Factors, 454–460 (Kluwer Academic Publishers, Dordrecht, 2004).
59. Parkinson, N. G. et al. Crystal and magnetic structures of $A_2YRu_{1-x}Cu_xO_6$ with A = Sr, Ba and x = 0.05 to 0.15. *J. Mater. Chem.* **13**, 1468–1474 (2003).
60. Paddison, J. A. M. et al. Suppressed-moment 2-**k** order in the canonical frustrated antiferromagnet $Gd_2Ti_2O_7$. *npj Quantum Mater.* **6**, 99 (2021).
61. Fishman, R. S., Fernandez-Baca, J. A. & Rõõm, T. Spin-Wave Theory and its Applications to Neutron Scattering and THz Spectroscopy. 2053-2571 (Morgan and Claypool Publishers, 2018).
62. Ader, J.-P. Magnetic order in the frustrated Heisenberg model for the fcc type-I configuration. *Phys. Rev. B* **65**, 014411 (2001).
63. Toth, S. & Lake, B. Linear spin wave theory for single-**q** incommensurate magnetic structures. *J. Phys.Condens. Matter* **27**, 166002 (2015).
64. Toth, S., Lake, B., Ward, S. & Le, M. D. SpinW program. Available from https://github.com/spinw/spinw.
65. Dahlbom, D. et al. Renormalized classical theory of quantum magnets. arXiv:2304.03874 (2023).
66. Wildes, A. R., Rule, K. C., Bewley, R. I., Enderle, M. & Hicks, T. J. The magnon dynamics and spin exchange parameters of $FePS_3$. *J. Phys. Condens. Matter* **24**, 416004 (2012).
67. Stone, M. B., Ehlers, G. & Granroth, G. E. S = 2 quasi-one-dimensional spin waves in $CrCl_2$. *Phys. Rev. B* **88**, 104413 (2013).
68. Pitcairn, J. et al. Low-dimensional metal–organic magnets as a route toward the S = 2 Haldane phase. *J. Am. Chem. Soc* **145**, 1783–1792 (2023).
69. Rau, J. G., McClarty, P. A. & Moessner, R. Pseudo-Goldstone gaps and order-by-quantum disorder in frustrated magnets. *Phys. Rev. Lett.* **121**, 237201 (2018).
70. Aczel, A. A. et al. Highly anisotropic exchange interactions of $j_{\rm eff} = \frac{1}{2}$ iridium moments on the fcc lattice in La_2BIrO_6(B = Mg, Zn). Phys. Rev. B 93, 214426 (2016).
71. Kaplan, T. A. Frustrated classical Heisenberg model in one dimension with nearest-neighbor biquadratic exchange: Exact solution for the ground-state phase diagram. *Phys. Rev. B* **80**, 012407 (2009).
72. Wang, Z., Zhang, P. & Shi, J. Orbital magnetization and its effect in antiferromagnets on the distorted fcc lattice. *Phys. Rev. B* **76**, 094406 (2007).
73. Kikuchi, K., Miyadai, T., Fukui, T., Itô, H. & Takizawa, K. Spin structure and magnetic properties of NiS_2. *J. Phys. Soc. Jpn* **44**, 410–415 (1978).
74. Yosida, K. & Inagaki, S. Consideration on four-spin exchange interactions in fcc spin lattice with particular reference to NiS_2. *J. Phys. Soc. Jpn* **50**, 3268–3277 (1981).
75. Higo, T. & Nakatsuji, S. Magnetization anomaly due to the non-coplanar spin structure in NiS_2. *J. Phys. Soc. Jpn* **84**, 053702 (2015).
76. Burlet, P. et al. Noncollinear magnetic structure of $MnTe_2$. *Phys. Rev. B* **56**, 14013–14018 (1997).
77. Frazer, B. C., Shirane, G., Cox, D. E. & Olsen, C. E. Neutron-diffraction study of antiferromagnetism in UO_2. *Phys. Rev.* **140**, A1448–A1452 (1965).
78. Faber, J. & Lander, G. H. Neutron diffraction study of UO_2: Antiferromagnetic state. *Phys. Rev. B* **14**, 1151–1164 (1976).
79. Caciuffo, R. et al. Magnetic excitations and dynamical Jahn-Teller distortions in UO_2. *Phys. Rev. B* **59**, 13892–13900 (1999).
80. Dudarev, S. L. et al. Parametrization of LSDA + U for noncollinear magnetic configurations: Multipolar magnetism in UO_2. *Phys. Rev. Mater.* **3**, 083802 (2019).
81. Kermarrec, E. et al. Frustrated fcc antiferromagnet Ba_2YOsO_6: Structural characterization, magnetic properties, and neutron scattering studies. *Phys. Rev. B* **91**, 075133 (2015).
82. Maharaj, D. D. et al. Spin gaps in the ordered states of La_2LiXO_6(X = Ru, Os) and their relation to the distortion of the cubic double perovskite structure in $4d^3$ and $5d^3$ magnets. *Phys. Rev. B* **98**, 104434 (2018).
83. Heinonen, O., Heinonen, R. A. & Park, H. Magnetic ground states of a model for MNb_3S_6 (M = Co, Fe, Ni). *Phys. Rev. Mater.* **6**, 024405 (2022).
84. Pohle, R., Shannon, N. & Motome, Y. Spin nematics meet spin liquids: exotic quantum phases in the spin-1 bilinear-biquadratic model with Kitaev interactions. *Phys. Rev. B* **107**, L140403 (2023).
85. Wang, J. & Liu, Z.-X. Effect of ring-exchange interactions in the extended Kitaev honeycomb model. *Phys. Rev. B* **108**, 014437 (2023).
86. Gastiasoro, M. N., Eremin, I., Fernandes, R. M. & Andersen, B. M. Scanning tunnelling spectroscopy as a probe of multi-**q** magnetic states of itinerant magnets. *Nat. Commun.* **8**, 14317 (2017).
87. Rodríguez-Carvajal, J. Fullprof. 2k, version 4.6 c–Mar 2002. *Phys. B* **55**, 192 (1993).
88. Rodríguez-Carvajal, J. Recent advances in magnetic structure determination by neutron powder diffraction. *Phys. B* **192**, 55–69 (1993).
89. Caglioti, G., Paoletti, A. & Ricci, F. Choice of collimators for a crystal spectrometer for neutron diffraction. *Nuc. Instrum.* **3**, 223–228 (1958).
90. James, F. & Roos, M. Minuit - A system for function minimization and analysis of the parameter errors and correlations. *Comp. Phys. Commun.* **10**, 343–367 (1975).
91. James, F. MINUIT Function Minimization and Error Analysis: Minimization and Error Analysis: Reference Manual Version 94.1. CERN (1994). Available from https://cds.cern.ch/record/2296388/files/minuit.pdf.

Acknowledgements

This work was supported by the U.S. Department of Energy, Office of Science, Basic Energy Sciences, Materials Sciences and Engineering Division. This research used resources at the Spallation Neutron Source, a DOE Office of Science User Facility operated by the Oak Ridge National Laboratory.

Author contributions

J.A.M.P. analyzed the data and wrote the paper with input from all co-authors. J.Y. synthesized the samples and performed bulk characterization measurements. M.A.M. performed X-ray diffraction measurements. M.B.S., A.D.C., S.-H.D., S.G. and J.A.M.P. performed neutron-scattering experiments. M.J.C. and J.A.M.P. developed spin-wave fitting code. H.Z., D.D., K.B. and C.D.B. calculated spin-wave renormalization. A.D.C., C.D.B. and J.A.M.P. designed the study.

Competing interests

The authors declare no competing interests.

Additional information

Supplementary information The online version contains supplementary material available at https://doi.org/10.1038/s41535-024-00650-6.

Correspondence and requests for materials should be addressed to Joseph A. M. Paddison or Andrew D. Christianson.